Dynamical Mechanisms of Vortex Pinning in Superfluid Thin Films

Oliver R. Stockdale, Matthew T. Reeves,* and Matthew J. Davis
ARC Centre of Excellence in Future Low-Energy Electronics Technologies, School of Mathematics and Physics, University of Queensland, Saint Lucia, Queensland 4072, Australia

(Received 23 February 2021; revised 15 September 2021; accepted 14 November 2021; published 14 December 2021)

We characterize the mechanisms of vortex pinning in a superfluid thin film described by the two-dimensional Gross-Pitaevskii equation. We consider a vortex "scattering experiment" whereby a single vortex in a superfluid flow interacts with a circular, uniform pinning potential. By an analogy with linear dielectrics, we develop an analytical hydrodynamic approximation that predicts vortex trajectories, the vortex fixed point and the unpinning velocity. We then solve the Gross-Pitaevskii equation to validate this model, and build a phase portrait of vortex pinning. We identify two different dynamical pinning mechanisms marked by distinctive phonon emission signatures: one enabled by acoustic radiation and another mediated by vortex dipoles nucleated within the pin. Relative to obstacle size, we find that pinning potentials on the order of the healing length are more effective for vortex capture. Our results could be useful in mitigating the negative effects of drag due to vortices in superfluid channels, in analogy to maximizing supercurrents in type-II superconductors.

DOI: 10.1103/PhysRevLett.127.255302

Introduction.—The pinning of topological defects plays an important role in many physical and biological systems including cardiac muscle [1,2], active matter [3], and liquid crystals [4]. In quantum fluids, such as superfluids and superconductors, the defects are quantized vortices. Their pinning and unpinning from potential barriers is crucial in determining the breakdown of dissipationless superflow [5]. For example, vortex pinning is important for preventing flux creep in high-T_c superconductors [6–8], corrections to the Berezinskii-Kosterlitz-Thouless transition in thin-film He-II [9–11], and manipulating flows in atomtronic devices [12–14]. Beyond these lab-based systems, sudden rotation "glitches" observed in neutron stars are hypothesized to involve an abrupt "avalanche" of vortices unpinning *en masse* from the star's outer crust [15–17]. Further, the recent achievement of room-temperature superfluids [18] has stimulated interest in harnessing superfluidity in future quantum technologies such as low-energy transistors [19]. Similar to superconductors, a better understanding of vortex pinning may allow for enhanced superfluid critical currents.

While vortex nucleation is well understood in terms of Landau's critical velocity [20–23], the subsequent mechanisms for vortex pinning and unpinning still lack a complete theoretical description. For finite temperature systems which can be modeled by, e.g., Ginzburg-Landau equations [3,8] or two-fluid models [24], a vortex will be gradually attracted to a (stable) dynamical fixed point through the dissipative action of the normal fluid component. However, this cannot explain how pinning occurs in a pure superfluid with minimal thermal friction, a regime in which experiments now routinely operate [25–28]. This poses the question: What are the microscopic mechanisms for vortex pinning in a pure superfluid system?

In this Letter, we theoretically and numerically study vortex pinning via a vortex "scattering experiment" within a zero temperature superfluid, where a single vortex interacts with a circular pinning potential [Fig. 1]. We develop an analytical hydrodynamic approximation to describe the vortex dynamics, finding excellent agreement with Gross-Pitaevskii simulations at low velocities. At higher velocities, we identify two mechanisms of vortex pinning, which are clearly distinguished by the acoustic energy signals produced during the pinning process. Finally, we construct a phase diagram of the pinning process and find that larger obstacles are comparatively ineffective for vortex capture relative to their size.

Model.—We consider a weakly interacting Bose gas described by the Gross-Pitaevksii equation (GPE) $i\hbar\partial_t\psi(\mathbf{r},t) = \delta H/\delta\psi^*$ with Hamiltonian

$$H = \int \mathrm{d}\mathbf{r}\left(\frac{\hbar^2}{2m}|\nabla\psi(\mathbf{r},t)|^2 + V(\mathbf{r})|\psi(\mathbf{r},t)|^2 + \frac{g}{2}|\psi(\mathbf{r},t)|^4\right), \tag{1}$$

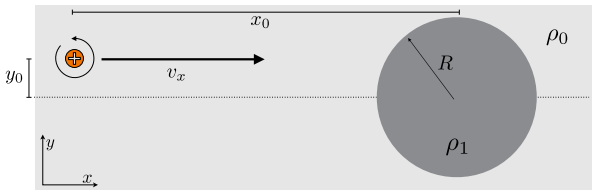

FIG. 1. Vortex scattering: A superfluid with background density ρ_0 flows uniformly with velocity v_x. Embedded in the flow is a single vortex initially located at (x_0, y_0). It encounters a circular pinning potential of radius R at the origin with density $\rho_1 < \rho_0$.

where g characterizes the repulsive particle interactions and m is the particle mass. We assume tight confinement along the z axis such that the problem effectively becomes two dimensional [29,30]. The superfluid flows along the x direction with background velocity v_x, past a stationary pinning potential $V(\mathbf{r}) = V_0(1 + \tanh[(R - |\mathbf{r}|)/w])/2$, with strength V_0, radius R, and boundary width $w \ll R$. A vortex is initialized at $\mathbf{r}_0 = (x_0, y_0)$, where y_0 defines the impact parameter of the scattering problem [Fig. 1].

Hydrodynamic approximation.—We first consider a hydrodynamic approximation for the vortex dynamics. This approach is valid for large ($R \gg \xi$) and weak pins ($V_0 \ll \mu$), and slow velocities ($v_x \ll c$), where $\xi = \hbar/\sqrt{m\mu}$ is the healing length, $\mu = n_0 g$ is the chemical potential, and $c = \sqrt{\mu/m}$ is the speed of sound.

Under the Madelung transformation $\psi(\mathbf{r}) = \sqrt{\rho/m}e^{i\Phi}$, the GPE can be recast to hydrodynamic equations governing the superfluid density $\rho(\mathbf{r})$ and velocity field $\mathbf{u}(\mathbf{r}) = \hbar\boldsymbol{\nabla}\Phi/m$ with phase $\Phi(\mathbf{r})$ [30]. The dynamics of a single (positive) vortex are then expressed exactly in terms of the phase and density gradients [31,32]

$$\dot{\mathbf{r}}_0 = \mathbf{u}_\Phi + \mathbf{u}_\rho \equiv \frac{\hbar}{m}\left(\nabla\Phi|_{\mathbf{r}_0} - \frac{1}{2}\hat{\mathbf{z}} \times \boldsymbol{\nabla}\ln\rho|_{\mathbf{r}_0}\right). \quad (2)$$

The gradients are evaluated at the vortex position, neglecting the (singular) self-contribution. A steady flow with $\dot{\mathbf{r}}_0 = \mathbf{0}$ must satisfy the mass continuity and vorticity quantization conditions

$$\boldsymbol{\nabla}\cdot\mathbf{J} = 0, \qquad (\nabla\times\mathbf{u})_z = \Gamma\delta(\mathbf{r} - \mathbf{r}_0), \quad (3)$$

where $\mathbf{J}(\mathbf{r}) \equiv \rho(\mathbf{r})\mathbf{u}(\mathbf{r})$ and $\Gamma \equiv h/m$ is the quantum of circulation. For $R \gg w \gtrsim \xi$, we may neglect the density gradients far from the obstacle boundary, and approximate the density as a step function, $\rho(\mathbf{r}) = \rho_0$ for $r > R$ and $\rho(\mathbf{r}) = \rho_0(1 - V_0/\mu)$ for $r < R$. Because of the two-dimensional nature of the problem, it may be solved by a direct correspondence with electromagnetism; defining $\mathbf{D} = -\hat{\mathbf{z}}\times\mathbf{u}$, $\mathbf{E} = -\hat{\mathbf{z}}\times\mathbf{J}/\rho_0$, and $\varepsilon(\mathbf{r}) = \rho_0/\rho(\mathbf{r})$ with $\mathbf{D}(\mathbf{r}) = \varepsilon(\mathbf{r})\mathbf{E}(\mathbf{r})$, Eqs. (3) take the same form as Maxwell's equations in linear dielectric media. The inverse density assumes the role of the relative permittivity, and vorticity that of the free charge [33]. The imposed flow corresponds to the displacement field for a dielectric cylinder within a uniform electric field. Thus, the imposed background flow is $\mathbf{u}_{\rm im} = \hbar\nabla\Phi_{\rm im}/m$, where

$$\frac{\hbar}{m}\Phi_{\rm im}(r,\theta) = \begin{cases} \frac{2\Upsilon v_x}{(\Upsilon+1)} r\cos\theta, & r < R; \\ v_x\left(1 + \frac{\Upsilon-1}{\Upsilon+1}\frac{R^2}{r^2}\right) r\cos\theta, & r \geq R, \end{cases} \quad (4)$$

where $\Upsilon = \rho_0/\rho_1$. The flow is uniform inside the obstacle and enhanced from the background value v_x by $2\Upsilon/(\Upsilon+1) \geq 1$. Outside, the result is similar to the solution for an impenetrable cylinder, which is recovered as $\Upsilon \to \infty$.

The velocity due to the vortex-pin interaction may be solved via the method of images. The solution is [34]

$$\frac{\hbar}{m}\nabla\Phi_v = \mathbf{u}_v(r) = -\frac{\Gamma}{2\pi}\left(\frac{\Upsilon-1}{\Upsilon+1}\right)\left(\frac{1}{d} - \frac{\Theta(r-R)}{r}\right)\hat{\boldsymbol{\theta}}, \quad (5)$$

where $\hat{\boldsymbol{\theta}}$ is the unit azimuthal vector, $d(r,R) = |R^2 - r^2|/r$ is the distance from the vortex to its image located at the inverse point $\bar{\mathbf{r}} = R^2\mathbf{r}/|r|^2$, and $\Theta(x)$ is the Heaviside step function. While Eq. (5) diverges at $r = R$ due to neglecting the vortex core, this may be remedied by the replacement $d \to \sqrt{d^2 + \delta^2}$. The phenomenological screening parameter δ is expected to be $\delta \gtrsim \xi$, limiting the induced velocity to $|\mathbf{u}_v| < c$, as required for a fluid of finite compressibility [39].

Pinning is enabled by the existence of a fixed point $\mathbf{r}_f$, where $\mathbf{u}_{\rm im}(\mathbf{r}_f) + \mathbf{u}_v(\mathbf{r}_f) + \mathbf{u}_\rho(\mathbf{r}_f) = \mathbf{0}$. The fixed point is located at $\mathbf{r}_f = \mathbf{0}$ when $v_x = 0$. As v_x increases $|\mathbf{r}_f|$ will approach R, and eventually vanish, causing the vortex to unpin. Since this occurs when $|\mathbf{r}_f| \approx R$, both density and phase gradients are important. Provided $w \gtrsim \xi$, then $\mathbf{u}_\rho$ may be approximated using the Thomas-Fermi solution $\rho(\mathbf{r}) = \rho_0[1 - V(\mathbf{r})/\mu]$. The largest density contribution, $\max[\mathbf{u}_\rho(\mathbf{r})]$, occurs at $r = R + w\log(1 - V_0/\mu)^{1/4} \approx R$, while $\max[\mathbf{u}_v(\mathbf{r})]$ occurs at exactly $r = R$. Within a logarithmic correction, we set $\dot{\mathbf{r}}_0 = \mathbf{0}$ at $\mathbf{r}_f = (R, -\pi/2)$ to obtain the critical unpinning velocity

$$u_c = \frac{\Gamma}{4\pi}\left(\frac{2w+\delta}{2w\delta}\right)\frac{V_0}{\mu}. \quad (6)$$

Notably, u_c is independent of R.

Since the density and image contributions both act to counteract the imposed flow, in Eq. (6) the term in parentheses may be interpreted as a reduced, *effective* screening parameter, $\delta_{\rm eff} = 2w\delta/(2w+\delta)$. Phenomenologically absorbing the density contributions into the effective screening $\delta_{\rm eff}$, we may obtain a closed form solution for the fixed point $\mathbf{r}_f$ against velocity. Balancing Eqs. (4) and (5) gives $\mathbf{r}_f = (r_f, \theta_f)$, with $\theta_f = -\pi/2$ and

$$r_f = \frac{1}{2}\left\{\sqrt{4R^2 + \left(\frac{\Gamma V_0}{4\pi v_x\mu}\right)^2 - \delta_{\rm eff}^2} - \sqrt{\left(\frac{\Gamma V_0}{4\pi v_x\mu}\right)^2 - \delta_{\rm eff}^2}\right\}. \quad (7)$$

Equation (7) bears a resemblance to the stagnation point solution in the classical Magnus effect [40]. Notice that Eq. (7) produces the same critical velocity as Eq. (6) (real solutions vanish above u_c).

The preceding (static) analysis may be applied to determine the vortex dynamics from Eq. (2) provided

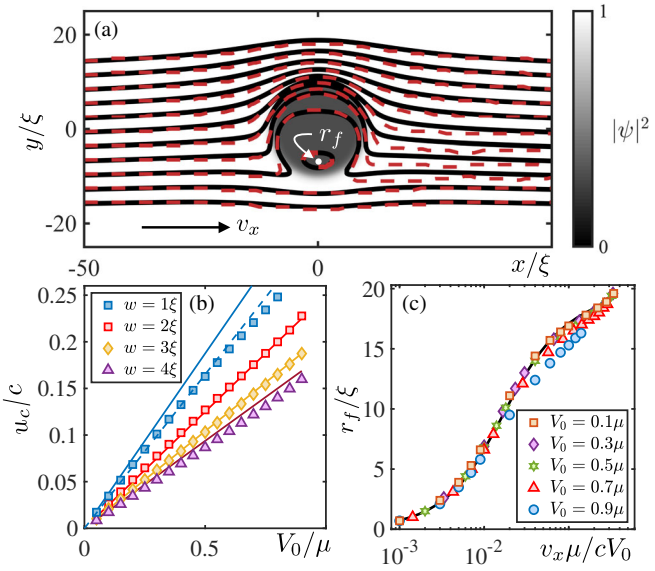

FIG. 2. Hydrodynamic theory and GPE comparison. (a) Vortex trajectories in the hydrodynamic theory (solid, black) and GPE (dashed, red) with $v_x = 0.1c$, $V_0 = 0.7\mu$, and $R = 10\xi$. (b) Unpinning velocity u_c vs obstacle strength V_0 for boundary widths w; solid lines show Eq. (6) with $\delta = 4.5\xi$ and $R = 20\xi$. Dashed line shows the correction $w \to w_{\text{eff}} = 1.2\xi$. (c) Fixed point radius r_f vs scaled flow velocity for $R = 20\xi$ and $w = \xi$. Points: GPE solutions; line: Eq. (7) with $\delta_{\text{eff}} = 1.5\xi$.

the velocities are small. Figure 2(a) shows excellent agreement between the hydrodynamic approximation for vortex trajectories and numerical GPE solutions for an example obstacle (for numerical methods, see Ref. [35]). The trajectories are asymmetric in y and may be open or closed depending on the initial location of the vortex. Within the hydrodynamic approximation, the open and closed trajectories do not overlap; the vortex is thus only pinned if it is initialized on a closed trajectory inside the pin.

Figure 2(b) compares the unpinning velocity u_c determined by GPE simulations [35] to the predictions of Eq. (6). We find good agreement between the two for a fixed value $\delta = 4.5\xi$. The agreement is excellent for $w/\xi \sim 2$–3, where the assumption $\xi \lesssim w \ll R$ is valid, but poorer for $w = \xi$ due to a breakdown of the Thomas-Fermi approximation; however, maintaining $\delta = 4.5\xi$ and replacing $w \to w_{\text{eff}} \approx 1.2\xi$, yields excellent agreement (equivalent to $\delta_{\text{eff}} \approx 1.56\xi$, dashed line).

In Fig. 2(c) we compare the location of the fixed point r_f against the prediction Eq. (7). By scaling the background velocity with the strength of the pinning potential, the data collapse onto a single curve, with $\delta_{\text{eff}} \approx 1.5\xi$. The results begin to deviate for $V_0 = 0.9\mu$, where the assumption $V_0 \ll \mu$ is no longer valid [35]. The value $\delta_{\text{eff}} = 1.5\xi$ obtained in Fig. 2(c) is in good agreement with the best-fit observed slope of u_c determined in Fig. 2(b) ($\delta_{\text{eff}} = 1.56\xi$).

Transition to pinning.—The hydrodynamic approach explains the conservative vortex trajectories and the mechanism for vortex unpinning. However, it cannot describe the dynamics of vortex pinning, where a vortex transitions from an open trajectory to a closed trajectory. We have therefore numerically simulated vortex scattering using the GPE over a wide range of parameters to identify how pinning occurs. To understand the dynamics of pinning, we consider the energy exchange in the system. Equation (1) may be written as $H = E_{\text{kin}} + E_{\text{pot}} + E_{\text{int}}$ describing the kinetic, potential, and interaction energies, respectively. The kinetic term may be further decomposed into incompressible and compressible components [41]; the incompressible part is associated with vortices, while the compressible part is due to sound waves [30].

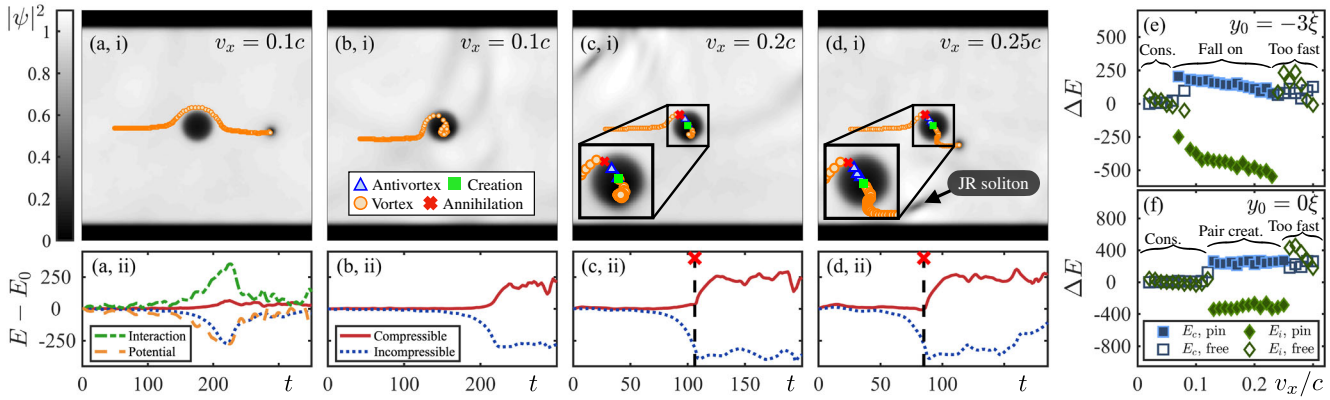

FIG. 3. Regimes of vortex pinning and scattering for a pinning potential of radius $R = 4\xi$ and strength $V_0 = \mu$ ($w = 2$): (a) Conservative, (b) fall-on, (c) pair creation, and (d) too fast, (see text). (i) Superfluid density at the end of the simulation. Markers show positions of vortices (orange circles) and antivortices (blue triangles) at equally spaced times in the dynamics. For simulation movies, see Supplemental Material [35]. (ii) Corresponding energy exchange curves vs time for the simulations shown in (i). Vertical dashed lines indicate an annihilation event. For clarity, only the most relevant energy curves are displayed. Note the total energy is conserved. (e),(f) Change in compressible (blue squares) and incompressible (green diamonds) kinetic energy vs v_x for impact factors (e) $y_0 = -3\xi$ and (f) $y_0 = 0\xi$. Solid points: vortex capture; hollow points: no capture.

We find that vortex scattering can be broadly classified into four regimes, characterized by different vortex trajectories and signatures of energy exchange. Examples of each regime are shown in Fig. 3 for an obstacle with $R = 4\xi$ and $V_0 = \mu$. Figures 3(a)–3(d), i show typical vortex trajectories, while Figs. 3(a)–3(d), ii show the salient features of energy exchange. Note the total energy is conserved in the simulations.

1. Conservative (no pinning). For a low background velocity $v_x = 0.1c$ and $y_0 = 0$, the vortex moves quasiadiabatically around the pinning potential [Fig. 3(a),i]. The trajectories qualitatively follow the hydrodynamic curves [Fig. 2(a)] and there is a near-reversible exchange between the energy components [Fig. 3(a),ii]. A small amount of energy is irreversibly lost to acoustic radiation, which slightly deflects the vortex from its hydrodynamic trajectory. This loss reduces as v_x decreases; for sufficiently low v_x, no pinning occurs regardless of initial conditions.

2. Fall-on (pinning). For the same background velocity ($v_x = 0.1c$) but a sufficiently negative impact parameter ($y_0 = -4\xi$), the vortex falls onto the pinning potential and enters a closed orbit [Fig. 3(b),i]. The fall-on is accompanied by an exchange between incompressible (vortex) and compressible (sound) kinetic energies [Fig. 3(b),ii]. The occurrence of this regime, which strongly depends on the value of y_0, can be understood from the trajectories of the hydrodynamic theory [Fig. 2(a)]. For $-R \lesssim y_0 < 0$, the trajectories exhibit high curvature implying a large acceleration. Similar to point charges, the energy radiated as sound by a line vortex is proportional to its acceleration [42]. These highly curved trajectories produce sufficient radiation to deflect the vortex onto a pinned orbit.

3. Pair creation (pinning). At larger velocities pinning may occur by a qualitatively different process. As shown in Fig. 3(c),i for $v_x = 0.2c$ and $y_0 = 0$, the incident vortex can induce the formation of a vortex-antivortex pair within the pinning potential as it approaches. The incident vortex then annihilates with the spawned antivortex, marked by a larger and more rapid burst of sound energy [Fig. 3(c),ii] than the fall-on regime. The pinned vortex is not the original vortex, but the (same-sign) vortex which spawned inside the pinning potential [Fig. 3(c),i].

4. Too fast (no pinning). For sufficiently large v_x (but $v_x < u_{\mathrm{crit}}$), pinning is no longer possible. The process of pair creation still occurs, but insufficient energy is radiated for the remaining vortex to be pinned and it instead escapes into the bulk [Fig. 3(d),i], recovering incompressible energy [Fig. 3(d),ii]. The acoustic pulse generated by the annihilation does not always disperse into ordinary phonons; in some cases, it creates a localized, nonlinear sound pulse, known as a Jones-Robert soliton [39] [Fig. 3(d),ii].

The fall-on and pair creation mechanisms are quantitatively distinct in terms of their acoustic emission signatures. In Fig. 3, we show the change in the compressible and incompressible kinetic energies against v_x for the impact parameters (e) $y_0 = -3\xi$ and (f) $y_0 = 0\xi$, which exhibit the fall-on and pair creation pinning regimes, respectively. In the fall-on regime [Fig. 3(e)], increasing v_x reduces the curvature of the vortex trajectories [cf. Fig. 2(a)] as the imposed flow dominates over the velocities induced by the pin. The amount of acoustic radiation therefore *decreases* with increasing velocity, until the amount emitted is no longer sufficient to deflect the vortex onto a pinned trajectory. By contrast, the threshold velocity for pair creation is larger than for fall-on, and the acoustic energy production is nearly constant in v_x [Fig. 3(f)]. At the transition to the "too fast" regime in both instances, the vortex fixed point exists, but within the boundary layer. Pinning thus becomes increasingly difficult as phonons can easily knock the vortex into the bulk.

Finally, in addition to v_x and y_0, the pinning dynamics also strongly depend on the pinning potential parameters. In Fig. 4 we plot the pinning phase diagram as a function of v_x and y_0 for the potential radii $R = \{4, 20\}\xi$ and strengths $V_0 = \{0.7, 1.0\}\mu$. The phase diagrams show that only a finite range of velocities lead to pinning. At low v_x, a vortex can become pinned even when the impact parameter exceeds the pinning potential radius, i.e., $y_0 < -R$ [Fig. 4(a)]. The $y_0 < 0$ region of parameter space is dominated by the "fall-on" regime due to the large curvature of trajectories. Conversely, vortices approaching from $y_0 > 0$ may only become pinned via the pair creation mechanism as described above. This distinction can be understood in terms of a destructive ($y_0 < 0$) and constructive ($y_0 \geq 0$) vector sum of the vortex velocity field and the imposed flow field (see Ref. [35]).

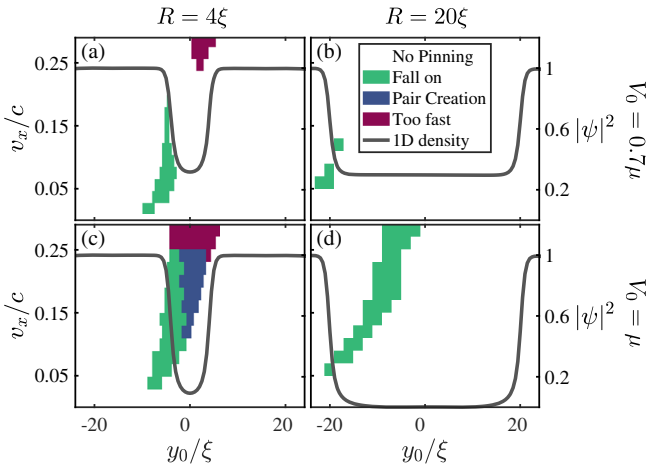

FIG. 4. Vortex pinning phase diagrams as a function of impact factor y_0 and background superfluid velocity v_x for pinning potentials with $R/\xi = \{4, 20\}$ (columns) and $V_0/\mu = \{0.7, 1\}$ (rows), respectively. The shaded regions represent pinning regimes (left y axis) and the gray lines represent the initial superfluid density along $x = 0$ at the location of the pinning potential (right y axis).

For $V_0 < \mu$, increasing V_0 significantly increases the likelihood of pinning [43]. The reduced superfluid density inside the pinning potential lowers the energy cost for pair creation, allowing it to occur over a wider range of parameters [Fig. 4(c), cf. Fig. 4(a)]. Further, we find that pinning potentials of smaller radii have a larger capture area relative to their size—for large radii, pinning does not occur at any V_0 for $y_0 > 0$ [Figs. 4(b) and 4(d)]. While large radii potentials provide a deep energy minimum [35], the pinned vortex states are less accessible dynamically; the larger radius vortex trajectories have a smaller acceleration and hence radiate less energy as sound, meaning that a relatively smaller region of phase space leads to pinning.

Conclusions and outlook.—We have considered the scattering of a quantized vortex off a repulsive pinning potential in a superfluid thin film. The hydrodynamic approximation describes the low velocity trajectories, as well as the location of the vortex fixed point and the unpinning velocity. Our predictions could be readily tested in ultracold atom experiments employing configurable optical potentials [44]. Radially inhomogeneous pins, which may be considered by analogy with antennae and waveguides in the dielectric analogy [45,46], could give different density and phase contributions that may lead to more effective pinning.

The GPE simulations identified two distinct pinning mechanisms, each marked by a characteristic emission of sound energy. In the pinning phase diagram we found that strong yet small radii potentials have a larger capture area compared to their size, being able to capture vortices at both positive and negative impact parameters. This may have important implications for devices utilizing superfluid helium thin films [28,47], where $\xi \sim 1$ Å. Our results suggest that atomic defects may be superior pins to fabricated, microscale defects; an array of small pins may prove more effective than a large pin occupying the same area. Like in superconducting devices, superfluid vortex pinning will likely play an important role in capturing free vortices and suppressing the breakdown of lossless flow in devices leveraging superfluidity.

We thank Arghavan Safavi-Naini and Mark Baker for useful discussions, and Andrew Groszek, Chris Baker, and Lewis Williamson for a critical reading of the manuscript. This research was supported by the Australian Research Council Centre of Excellence in Future Low-Energy Electronics Technologies (Project No. CE170100039) and funded by the Australian government.

*m.reeves@uq.edu.au

[1] J. M. Davidenko, A. V. Pertsov, R. Salomonsz, W. Baxter, and J. Jalife, Nature (London) **355**, 349 (1992).
[2] A. Pumir and V. Krinsky, J. Theor. Biol. **199**, 311 (1999).
[3] D. Pazó, L. Kramer, A. Pumir, S. Kanani, I. Efimov, and V. Krinsky, Phys. Rev. Lett. **93**, 168303 (2004).
[4] M. G. Campbell, M. Tasinkevych, and I. I. Smalyukh, Phys. Rev. Lett. **112**, 197801 (2014).
[5] L. A. K. Donev, L. Hough, and R. J. Zieve, Phys. Rev. B **64**, 180512(R) (2001).
[6] D. R. Nelson and V. M. Vinokur, Phys. Rev. B **48**, 13060 (1993).
[7] G. Blatter, M. V. Feigel'man, V. B. Geshkenbein, A. I. Larkin, and V. M. Vinokur, Rev. Mod. Phys. **66**, 1125 (1994).
[8] W.-K. Kwok, U. Welp, A. Glatz, A. E. Koshelev, K. J. Kihlstrom, and G. W. Crabtree, Rep. Prog. Phys. **79**, 116501 (2016).
[9] S. G. Hegde and W. I. Glaberson, Phys. Rev. Lett. **45**, 190 (1980).
[10] V. Ambegaokar, B. I. Halperin, D. R. Nelson, and E. D. Siggia, Phys. Rev. B **21**, 1806 (1980).
[11] P. W. Adams and W. I. Glaberson, Phys. Rev. B **35**, 4633 (1987).
[12] P. Kuopanportti and M. Möttönen, J. Low Temp. Phys. **161**, 561 (2010).
[13] T. W. Neely, A. S. Bradley, E. C. Samson, S. J. Rooney, E. M. Wright, K. J. H. Law, R. Carretero-González, P. G. Kevrekidis, M. J. Davis, and B. P. Anderson, Phys. Rev. Lett. **111**, 235301 (2013).
[14] E. C. Samson, K. E. Wilson, Z. L. Newman, and B. P. Anderson, Phys. Rev. A **93**, 023603 (2016).
[15] P. W. Anderson and N. Itoh, Nature (London) **256**, 25 (1975).
[16] R. I. Epstein and G. Baym, Astrophys. J. **328**, 680 (1988).
[17] L. Warszawski, A. Melatos, and N. G. Berloff, Phys. Rev. B **85**, 104503 (2012).
[18] G. Lerario, A. Fieramosca, F. Barachati, D. Ballarini, K. S. Daskalakis, L. Dominici, M. De Giorgi, S. A. Maier, G. Gigli, S. Kéna-Cohen, and D. Sanvitto, Nat. Phys. **13**, 837 (2017).
[19] A. V. Zasedatelev, A. V. Baranikov, D. Urbonas, F. Scafirimuto, U. Scherf, T. Stöferle, R. F. Mahrt, and P. G. Lagoudakis, Nat. Photonics **13**, 378 (2019).
[20] L. D. Landau, J. Phys. USSR **5**, 71 (1941).
[21] T. Frisch, Y. Pomeau, and S. Rica, Phys. Rev. Lett. **69**, 1644 (1992).
[22] B. Jackson, J. F. McCann, and C. S. Adams, Phys. Rev. A **61**, 051603(R) (2000).
[23] J. H. Jung, H. J. Kim, and Y. Shin, J. Korean Phys. Soc. **78**, 19 (2021).
[24] K. W. Schwarz, Phys. Rev. Lett. **47**, 251 (1981).
[25] D. I. Bradley, S. N. Fisher, A. M. Guénault, R. P. Haley, S. O'Sullivan, G. R. Pickett, and V. Tsepelin, Phys. Rev. Lett. **101**, 065302 (2008).
[26] M. Niemetz, R. Hänninen, and W. Schoepe, J. Low Temp. Phys. **187**, 195 (2017).
[27] G. Gauthier, S. S. Szigeti, M. T. Reeves, M. Baker, T. A. Bell, H. Rubinsztein-Dunlop, M. J. Davis, and T. W. Neely, Phys. Rev. Lett. **123**, 260402 (2019).
[28] Y. P. Sachkou, C. G. Baker, G. I. Harris, O. R. Stockdale, S. Forstner, M. T. Reeves, X. He, D. L. McAuslan, A. S. Bradley, M. J. Davis, and W. P. Bowen, Science **366**, 1480 (2019).
[29] S. J. Rooney, P. B. Blakie, B. P. Anderson, and A. S. Bradley, Phys. Rev. A **84**, 023637 (2011).

[30] A. S. Bradley and B. P. Anderson, Phys. Rev. X **2**, 041001 (2012).
[31] O. Törnkvist and E. Schröder, Phys. Rev. Lett. **78**, 1908 (1997).
[32] A. J. Groszek, D. M. Paganin, K. Helmerson, and T. P. Simula, Phys. Rev. A **97**, 023617 (2018).
[33] D. A. Browne and S. Doniach, Phys. Rev. B **25**, 136 (1982).
[34] W. Smythe and W. Smythe, *Static and Dynamic Electricity*, International Series in Pure and Applied Physics (McGraw-Hill, New York, 1950).
[35] See Supplemental Material at http://link.aps.org/supplemental/10.1103/PhysRevLett.127.255302, which includes Refs. [36–38] for full details of the numerical methods, more details regarding the calculation of the vortex fixed point, a calculation of the energy of a pinned vortex, further discussion of the vortex pair creation mechanism, and movies showing examples of the four vortex scattering regimes and the stationary states of a vortex trapped on the pinning potential as a function of increasing superfluid flow velocity.
[36] P. Coleman, *Introduction to Many-Body Physics* (Cambridge University Press, Cambridge, England, 2015).
[37] N.-E. Guenther, P. Massignan, and A. L. Fetter, Phys. Rev. A **96**, 063608 (2017).
[38] G. R. Dennis, J. J. Hope, and M. T. Johnsson, Comput. Phys. Commun. **184**, 201 (2013).
[39] C. A. Jones and P. H. Roberts, J. Phys. A **15**, 2599 (1982).
[40] G. K. Batchelor, *An Introduction to Fluid Dynamics*, Cambridge Mathematical Library (Cambridge University Press, Cambridge, England, 2000).
[41] C. Nore, M. Abid, and M. E. Brachet, Phys. Rev. Lett. **78**, 3896 (1997).
[42] W. F. Vinen, Phys. Rev. B **64**, 134520 (2001).
[43] For $V_0 \geq \mu$, the pinning diagram does not change significantly.
[44] G. Gauthier, I. Lenton, N. M. Parry, M. Baker, M. J. Davis, H. Rubinsztein-Dunlop, and T. W. Neely, Optica **3**, 1136 (2016).
[45] A. Vigants and S. P. Schlesinger, IRE Trans. Microwave Theory Tech. **10**, 375 (1962).
[46] E. Yamashita, K. Atsuki, and Y. Nishino, IEEE Trans. Microwave Theory Tech. **29**, 987 (1981).
[47] E. Varga, V. Vadakkumbatt, A. J. Shook, P. H. Kim, and J. P. Davis, Phys. Rev. Lett. **125**, 025301 (2020).